Resolution Enhancement by Compressive Sensing in Power Quality and Phasor Measurement

Matteo Bertocco, *Member, IEEE*, Guglielmo Frigo, Claudio Narduzzi, *Member, IEEE*, and Federico Tramarin, *Member, IEEE*

***Abstract*— Measurement in power systems and, particularly, in smart grids and smart microgrids is often concerned with harmonic analysis of voltage and current waveforms. The use of Fourier-based algorithms is widespread, and the limits following from the fundamental time-versus-frequency tradeoff that relates observation time to frequency resolution are well understood. This paper presents the application of an algorithm based on the principles of compressive sensing that can achieve an order-of-magnitude resolution improvement without significantly extending total observation time. For harmonic analysis in power systems, this means that accurate results can be obtained using shorter observation intervals, which allow to effectively track changes and reduce the effect of transients on measurements. The application of the algorithm to harmonics and interharmonics, as well as to phasor measurement, is considered and analyzed.**

***Index Terms*— Compressive sensing (CS), harmonic analysis, power system measurement.**

I. Introduction

MEASUREMENT in power systems, particularly smart grids and microgrids, is often concerned with the analysis of voltage and current waveforms [1], [2], in which Fourier analysis plays a leading role. For instance, power quality analyzers (PQAs) can determine the harmonic content of current or voltage waveforms at selected points in a network [3], [4]. Phasor measurement units (PMUs) can also make use of Fourier-based algorithms to carry out time-synchronized measurements of phasors at the fundamental line frequency [5], [6], although the basic estimation model provided in IEEE Standard C37.118-2011 refers to a digital quadrature demodulator [7].

Any measurement algorithm based on the discrete Fourier transform (DFT) is characterized by a fundamental time-versus-frequency tradeoff. DFT coefficients obtained from a sequence of N samples, taken at uniform intervals T_s, are determined on a discrete frequency grid whose step size Δ_f is the reciprocal of the observation time NT_s. This determines the minimum theoretical frequency separation at which two waveform components can be discerned. To resolve harmonics of the power-line frequency, observation time would have to be equal to at least one waveform cycle, T_0.

Resolution and accuracy in DFT-based algorithms are affected by spectral leakage, which can be countered either by windowing of the sample sequence followed by frequency-domain interpolation of DFT coefficients, or by synchronization of the sampling rate to the line frequency. The former approach has been considered for phasor measurement [8]. The need to allow for window main-lobe width means that, in principle, a larger component separation would be necessary, resulting in longer observation times, of between two and four waveform cycles [9]. Reporting latency is also affected since, for any DFT-based algorithm, this cannot be shorter than half of the observation time.

One-cycle phasor estimators can be realized as well, as long as a very limited range of variation is allowed for the power-line frequency, so that inaccuracies due to residual leakage effects in off-nominal situations can be made small enough to be negligible [10]. This does not consider the possible presence of interharmonics, whose interference might affect phasor estimates.

Line-frequency synchronization is considered, for the measurement of harmonics and interharmonics, in IEC Standard 61000-4-7, where interharmonic components are dealt with by defining interharmonic groups [11]. As a 5-Hz frequency resolution is required, suggested observation time is 200 ms (equal to $10T_0$ for 50-Hz systems or $12T_0$ for 60-Hz systems), again showing that any resolution improvement has to be paid for by an increase in measurement time.

These well-known conditions determine basic limitations of the Fourier approach, particularly when dynamic conditions are considered. To overcome the shortcomings of the static signal model underlying Fourier analysis, different methods have been proposed, allowing phasor measurement [12], [13] and harmonic analysis [14] under dynamic conditions. These approaches were shown to be able to meet most or even all requirements for dynamic synchrophasor measurements, as specified in IEEE Standard C37.118-2011, but require longer measurement times [15], [16]. Recently, Prony's method was shown to have the potential for accurate synchrophasor estimation in a one-cycle observation interval [17].

Phasor and harmonic measurements are commonly related to HV and medium-voltage (MV) distribution grids. However, the emerging scenario of smart microgrids [18], [19] points to the pervasive use of intelligent meters in low-voltage (LV)

Manuscript received November 11, 2013; revised February 21, 2014; accepted April 10, 2014. The Associate Editor coordinating the review process was Dr. Lorenzo Peretto.

M. Bertocco, G. Frigo, and C. Narduzzi are with the Department of Information Engineering, University of Padova, Padova I-35131, Italy (e-mail: mat@dei.unipd.it; frigogug@dei.unipd.it; narduzzi@dei.unipd.it).

F. Tramarin is with the National Research Council of Italy, Institute of Electronics, Computer and Telecommunication, Padova I-35131, Italy (e-mail: tramarin@dei.unipd.it).

Color versions of one or more of the figures in this paper are available online at http://ieeexplore.ieee.org.

Digital Object Identifier 10.1109/TIM.2014.2321465

distribution grids, providing continuously updated measurements of phasors and power quality indexes for use, e.g., in distributed control. Low-cost measuring equipment is expected to provide accuracy performance indexes similar to those already achieved by PQAs and standard PMUs, but under more distorted and disturbed operating conditions, as experienced in LV distribution grids. At the same time, the need for fast reporting rates is emphasized.

This paper presents the application to harmonic analysis, interharmonic, and phasor measurement of an original approach based on application of the principles of compressive sensing (CS) to DFT-based waveform analysis, extending on the work already presented in [20]. The proposed CS-DFT algorithm can achieve an order-of-magnitude improvement in frequency grid resolution, compared with the DFT step size Δ_f, without significantly extending total observation time.

While its application does not eliminate spectral leakage, the algorithm significantly reduces scalloping loss effects, while long-range frequency interference are dealt with by jointly processing frequency-domain information when estimating waveform components [21]. Although still relying on a static signal model, the finer frequency grid of the CS-DFT algorithm allows to reduce the effects of dynamic conditions on measurement accuracy, so that requirements of IEEE Standard C37.118-2011 can mostly be met. As the algorithm is nonparametric, it can be made adaptable enough to provide either PQA or PMU measurements by a single device as the need arises.

This paper is organized as follows. A summary of the proposed CS approach to harmonic analysis is given in the next section. Some empirical results are presented in Section III to demonstrate the basic features of the algorithm, and then the significance of the proposed method for power quality and phasor measurement is discussed in Section IV, where the main contributions and results are presented. The more demanding aspects of dynamic behavior are considered in Section V, which is followed by some concluding remarks.

II. Fourier Analysis by CS

Consider a multisine waveform expressed by the sum of a number of complex exponential components (with suitable symmetries)

$$s(t) = \sum_h \left[\frac{A_h}{2} e^{j(\phi_h + 2\pi f_h t)} + \frac{A_h}{2} e^{-j(\phi_h + 2\pi f_h t)} \right]. \quad (1)$$

This equation can be referred to harmonic analysis, in which case $f_h = h \cdot f_0$ and $f_0 = 1/T_0$ is the fundamental frequency, as well as to a more general situation where no relationship among frequencies may exist, e.g., in the analysis of power system interharmonics.

Given a sequence of N waveform samples, the DFT algorithm provides a corresponding set of N frequency-domain coefficients that can be expressed by

$$S\left(\frac{k}{N}\right) = \sum_{h \in S_H} \frac{A_h}{2} e^{j\phi_h} D_N\left(\frac{k}{N} - \nu_h\right) e^{-j2\pi\left(\frac{k}{N} - \nu_h\right) n_0} \quad (2)$$

where $0 \le k < N$, $\nu_h = f_h T_s$ is the frequency of the hth waveform component normalized by the sampling rate $1/T_s$, and $D_N(\cdot)$ is the Dirichlet kernel

$$D_N(\nu) = \frac{\sin \pi N \nu}{N \sin \pi \nu} e^{-j\pi(N-1)\nu}. \quad (3)$$

Index n_0 refers to the time position of the first sample in the sequence, and will henceforth be set to zero.

DFT coefficients in (2) are given at discrete normalized frequency values $\nu = k/N$, i.e., for integer multiples of the frequency step $1/NT_s$. Hermitian symmetry implies that the sum in (2) extends to image components at normalized frequencies $1 - \nu_h$. In short, this is denoted by $h \in S_H$, where S_H is the set that includes all contributing complex exponential terms.

We now define a finer frequency grid, with a smaller step $\Delta'_f = \Delta_f / P$, so that the total number of grid points is $N' = P \cdot N$. The integer P can be called the interpolation factor. Referring waveform frequencies to this finer grid allows to express them as

$$\nu_h = \frac{l_h + \delta'_h}{N'} = \frac{l_h + \delta'_h}{P} \cdot \frac{1}{N} \quad (4)$$

for some integer $l_h \in [0, 1, \ldots, N' - 1]$, with $|\delta'_h| \le 1/2$. The closest approximation to ν_h on this new grid is

$$\hat{\nu}_h = \frac{l_h}{NP}. \quad (5)$$

Let $S_h \subset \{0,\ 1,\ \ldots,\ N' - 1\}$ be the subset of integers corresponding to waveform components, i.e., $l \in S_h$ implies $l = l_h$ for some value of the index h. Replacing ν_h by $\hat{\nu}_h$ allows to approximate (2) as

$$S\left(\frac{k}{N}\right) \simeq \sum_{\substack{l \in S_h \\ 0 \le l < N'}} \frac{A_h}{2} e^{j\phi_h} D_N\left(\frac{k}{N} - \frac{l}{N'}\right), \quad 0 \le k < N. \quad (6)$$

Of course, under our assumptions, the number of elements in S_h, i.e., its cardinality $|S_h|$, is the same as $|S_H|$. Equation (6) can be written in a more compact form as a matrix relationship between the frequency grid indexed by k (the DFT index) and the finer grid indexed by l

$$\mathbf{s} \simeq \mathbf{D}\mathbf{a}. \quad (7)$$

DFT coefficients are contained in vector $\mathbf{s}$ and elements of the $N \times N'$ matrix $\mathbf{D}$ are defined by $d_{k,l} = D_N(k/N - l/N')$. The unknown vector $\mathbf{a}$ contains complex amplitude values that can be associated to waveform components.

The actual measurement equation

$$\mathbf{x} = \mathbf{s} + \mathbf{n} = \mathbf{D}\mathbf{a} + \mathbf{e} \quad (8)$$

also accounts for measurement noise and uncertainty. Here, $\mathbf{x}$ is the vector of computed DFT coefficients, and it should be reminded that, if the additive random contribution affecting the N time-domain samples has variance σ_n^2, then $\mathbf{n}$ is a zero-mean uncorrelated random complex vector, with covariance $(\sigma_n^2/N)\mathbf{I}$, which turns out to be approximately Gaussian [22]. The vector $\mathbf{e}$ in the rightmost term summarizes both $\mathbf{n}$ and the approximation effect introduced by (5).

Given the vector $\mathbf{x}$, estimates of the components of $s(t)$ are the nonzero elements a_l in vector $\mathbf{a}$ contributing terms to summation (6), whose index values satisfy $l \in S_h$. Since $|S_h| \ll N'$, vector $\mathbf{a}$ is considered sparse, all its other elements being zero. S_h is called the support of $\mathbf{a}$.

In a nutshell, this is the problem feature that leads to considering a CS approach for Fourier analysis of the waveform measurement. The CS solution to (8) can be formulated as follows:

$$\hat{\mathbf{a}} = \arg\min_{\mathbf{a}} \|a\|_0 \quad \text{subject to: } \|\mathbf{x} - \mathbf{D}\mathbf{a}\|_2 \leq \epsilon \tag{9}$$

where $\|\mathbf{a}\|_0$ indicates the ℓ^0 pseudonorm, i.e., the number of nonzero elements of $\mathbf{a}$.

As (9) is known to have combinatorial complexity, in practice, $\hat{\mathbf{a}}$ is found either by convex relaxation (i.e., constrained minimization of the ℓ^1 norm $\|\mathbf{a}\|_1$ in place of $\|\mathbf{a}\|_0$), or by employing a so-called greedy algorithm. We shall follow the latter approach, which is computationally less demanding, using orthogonal matching pursuit (OMP) [23], [24] to recover the vector estimate $\hat{\mathbf{a}}$.

OMP is an iterative approximation algorithm whose steps are given as follows.

Step 1: The initial approximation residual $\mathbf{r}_0$ is equal to the measurement vector: $\mathbf{r}_0 = \mathbf{x}$, and the initial estimated support set is empty: $\hat{S}_0 = \varnothing$. We also introduce the matrix $\mathbf{D}_{S_t}$ that will be composed only of the columns of $\mathbf{D}$ selected through the steps of the algorithm. Initially, $\mathbf{D}_{S_0}$ has zero columns. The iteration counter is set to $t = 1$.

Step 2: Find the index l_t as

$$l_t = \arg\max_{0 \leq l < N'} \|\mathbf{D}^H \mathbf{r}_{t-1}\|_2 \tag{10}$$

where the superscript H denotes a complex conjugate transpose matrix. Iterations of this step cover the support recovery part of the algorithm.

Step 3: Augment the estimated support set: $\hat{S}_t = \hat{S}_{t-1} \cup \{l_t\}$. The column of $\mathbf{D}$ with the corresponding index is appended to the matrix: $\mathbf{D}_{S_t} = [\mathbf{D}_{S_{t-1}}\ \mathbf{d}_{l_t}]$.

Step 4: Calculate a new vector

$$\hat{\mathbf{a}}_{l_t} = \arg\min_{\mathbf{a}} \|\mathbf{x} - \mathbf{D}_{S_t}\mathbf{a}\|_2 = \left(\mathbf{D}_{S_t}^H \mathbf{D}_{S_t}\right)^{-1} \mathbf{D}_{S_t}^H \mathbf{x} \tag{11}$$

which has t nonzero elements. Iterations of this step provide a progressively refined estimate.

Step 5: Calculate the new residual: $\mathbf{r}_t = \mathbf{x} - \mathbf{D}_{S_t}\hat{\mathbf{a}}_{l_t}$, then increment the iteration counter: $t = t + 1$, and return to Step 2.

The OMP algorithm can have two stopping criteria:

1) if the number of nonzero elements of $\mathbf{a}$ is known in advance, the number of iterations t_{MAX} can be predefined: $t_{\mathrm{MAX}} = |S_h|$;
2) otherwise, the algorithm can be stopped when the approximation residual drops below a given threshold ϵ, as introduced by (9), in which case t_{MAX} is the first value of t that satisfies $\|\mathbf{r}_t\|_2 < \epsilon$, and the estimated cardinality of the support of $\mathbf{a}$ is $|\hat{S}_h| = t_{\mathrm{MAX}}$.

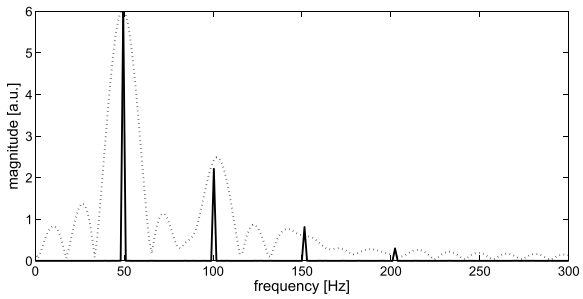

Fig. 1. Magnitude estimates of a four-harmonic waveform obtained by the CS-DFT algorithm. A zero-padded 256-point DFT (dotted) is plotted for comparison.

The resulting sparse vector $\hat{\mathbf{a}}_{t_{\mathrm{MAX}}}$ is the desired estimate of the components of (1). The important point is that, by defining a suitable approximation threshold, the algorithm can solve (9) without advance knowledge of the support cardinality $|S_h|$, although it may be useful to set a limiting number of OMP iterations as a safety criterion.

As discussed in [21], the required minimum frequency separation between two waveform components lying on the fine grid is approximately $1.5 \cdot \Delta_f = 1.5 \cdot (\Delta_l / P)$, where Δ_l is the integer difference between the fine-grid indexes of the two components. When this condition is satisfied, OMP correctly recovers the support S_h and amplitude estimates are accurate. Furthermore, the finer grid allows to estimate component frequencies to within $\pm(\Delta'_f/2)$.

It should be remembered, however, that the latter quantity cannot be made infinitely small by the expedient of increasing P at will. Matrix $\mathbf{D}$ represents the effect of spectral leakage, through values of the Dirichlet kernel computed on a suitable 2-D grid. When large values of the interpolation factor are considered, the numerical conditioning of $\mathbf{D}$ tends to get worse. Thus, it is advisable to aim at values of P not much larger than order of 10.

III. Measuring a Simple Harmonic Waveform

The proposed CS-DFT approach promises to achieve enhanced frequency accuracy without requiring an extension of the observation time, allowing to overcome the traditional time-versus-frequency tradeoff of DFT-based methods. The CS framework provides a rigorous and effective procedure to determine from the experimental data the support S_h on a fine frequency grid and, subsequently, reconstruct the composition of a waveform.

The example shown in Fig. 1 refers to the analysis of a periodic waveform composed of four harmonic terms. The initial phase of each component is independently drawn from a random uniform distribution in the interval $[0, 2\pi)$. Data record size is $N = 256$ samples, and the assumed sampling frequency is 4100 Hz. This results in a DFT frequency grid step $\Delta_f = 16.02$ Hz, while the finer frequency grid with an interpolation factor $P = 11$ is $\Delta'_f = 1.456$ Hz. With these parameters, the fundamental frequency $f_1 = 49.5$ Hz is an exact multiple of the fine-grid step: $f_1 = l_1 \Delta_f$, with $f_1 = 34$.

The minimum separation condition given in the previous section is satisfied, allowing OMP to correctly locate on the

TABLE I
CS-DFT ESTIMATION OF A FOUR-TERM HARMONIC WAVEFORM WITH SNR = 40 dB

Harmonic no.	**1**	**2**	**3**	**4**
Frequency [Hz]	49.50	99	148.51	198.01
Magnitude [a.u.]	6	2.21	0.812	0.299
Mean dev. (relative)	-4×10^{-5}	3×10^{-4}	3×10^{-4}	2×10^{-3}
Std. dev. (relative)	6×10^{-4}	1.5×10^{-3}	4×10^{-3}	1×10^{-2}
Phase [rad]	3.96	4.85	4.75	3.11
Mean dev. [rad]	1.2×10^{-4}	3×10^{-4}	-7×10^{-4}	-8×10^{-3}
Std. dev. [rad]	1.7×10^{-2}	2×10^{-2}	2×10^{-2}	2×10^{-2}

TABLE II
CS-DFT ESTIMATION OF A FOUR-HARMONIC WAVEFORM WITH SNR = 40 dB = OFF-GRID COMPONENTS

Harmonic no.	**1**	**2**	**3**	**4**
Frequency [Hz]	50	100	150	200
Magnitude [a.u.]	6	2.21	0.812	0.299
Mean dev. (relative)	5×10^{-4}	-5×10^{-3}	1×10^{-2}	9×10^{-2}
Std. dev. (relative)	1×10^{-2}	2×10^{-2}	2×10^{-2}	2.5×10^{-2}
Phase [rad]	6.01	5.54	0.16	3.91
Mean dev. [rad]	5×10^{-2}	9×10^{-2}	-1×10^{-1}	-1×10^{-1}
Std. dev. [rad]	2×10^{-2}	1.3×10^{-2}	1×10^{-2}	8×10^{-2}

fine grid the frequencies of the four components, with the corresponding magnitude estimates shown by the four sharp peaks in Fig. 1. For comparison, this figure also shows a plot of the magnitude of the DFT computed from a 256-point sample sequence, zero-padded with $(P-1)N$ zeroes. Since the latter is defined on the same finer grid as the CS-DFT, comparison readily evidences discrepancies and the adverse effects of interference among the waveform components that would affect any purely DFT-based estimate. In particular, for the second harmonic, the significant discrepancy in magnitude from the CS-DFT can be attributed to interference from the fundamental.

An assessment of CS-DFT measurement uncertainty for this example is presented in Table I, which summarizes the outcomes from a set of 100 simulation runs, where random white noise was added to the reference harmonic waveform. The assumed signal-to-noise ratio (SNR) = 40 dB can be considered representative of practical situations, where the equivalent number of bits of the waveform digitizer is low (e.g., an 8-bit analog-to-digital converter).

It can be seen that estimation bias is negligible when component frequencies fall on the fine grid. For all four harmonic components, the relative mean deviation from the reference values of magnitude and phase is almost one order of magnitude smaller than the relative standard deviation due to the presence of noise.

At SNR = 40 dB and with a coverage factor equal to three, uncertainty on the phasor magnitude of the fundamental component would be better than 0.2%. For phase estimates, estimation uncertainty is about 0.06 rad.

It has to be mentioned that, for the smaller components, noise may sometimes affect the outcome of the support recovery procedure. In a single case, out of 100 simulations, the frequency of the third harmonic component was not estimated correctly. The results reported in Table I for this component do not include the outcome of the simulation run where support recovery partly failed.

Harmonic frequencies in Table I were intentionally chosen to fall on the CS-DFT fine grid. However, the equality $\nu_1 = (l_1/NP)$ denotes a coherent sampling situation, where l_1 periods of the fundamental frequency are exactly contained in an interval of length NP. In practice, it can be more realistically assumed that the measuring device will be designed so that the observation interval approximately matches the condition given above, i.e., the CS-DFT algorithm will operate in quasi-coherent sampling conditions. The results presented in Table II reflect this assumption, as the fundamental frequency $f_1 = 50$ Hz differs from the previous case by just 1%. Of course, in this case, spectral leakage affects component estimates to some extent, introducing bias in magnitude due to scalloping loss and a limited amount of interference. To counter this, record length was set to $N = 256$ rather than the theoretical minimum $N = 128$, so that component frequency separation Δ_l/P is twice the limiting value given in Section II. Comparison with Table I shows that both the estimate mean deviation and the standard deviation are increased.

IV. APPLICATION TO POWER SYSTEMS

To show that power system applications are within the range of feasibility of the proposed CS-DFT algorithm, in the following, we shall consider in greater depth two suitable fields: 1) power quality analysis and 2) phasor measurement.

A. PQA—Harmonic and Interharmonic Measurement

The synchronized measurement approach of IEC Standard 61000-4-7 is well suited to test the CS approach, as far as harmonic and interharmonic measurement is concerned. A frequency grid step corresponding to the required resolution of 5 Hz could be obtained by the acquisition of even a single fundamental cycle of the waveform, using interpolation factor $P = 10$ (or $P = 12$). Accounting for the minimum separation constraint given in Section II, this would have to be increased to one and a half cycle.

It should be remembered that the IEC standard assumes an observation interval equal to an integer number of power-line cycles. Therefore, sampling frequency needs to be adjusted accordingly (e.g., by phase-lock techniques) if the fundamental frequency varies. For the purposes of this analysis, it is equivalent and simpler to refer to a static condition with exactly coherent sampling, as already done in the previous section. It is then possible to consider a degree of offset resulting in quasi-coherent sampling, although it seems reasonable to assume that, in this case, the measuring device would be designed to keep as close as possible to the ideal condition.

It should be noticed that interharmonics usually have far smaller magnitudes than some harmonic components, and therefore spectral interference due to the quasi-coherent sampling condition might have more significance. To counter

TABLE III
CS-DFT ESTIMATION OF INTERHARMONICS IN A FOUR-HARMONIC WAVEFORM

Harmonic no.	**1**	**2**	**3**	**4**
Frequency [Hz]	50.23	100.46	150.69	200.92
Magnitude [a.u.]	6	5.16	4.44	3.83
Interharmonic no.	**0.5**	**1.5**	**2.5**	**3.5**
Frequency [Hz]	34.58	58.60	121.94	167.80
Magnitude [a.u.]	0.51	0.39	0.59	0.31
Deviation (relative)	1.4×10^{-2}	-0.1×10^{-2}	-2×10^{-2}	0.1×10^{-2}
Phase [rad]	6.01	5.54	0.16	3.91
Deviation [rad]	0.16	0.1	-0.1	-0.2

this more effectively, the observation interval can be further lengthened.

Throughout this section, data record size is $N = 512$ samples and sampling frequency is 4100 Hz, which yields $NT_s \simeq 125$ ms, still almost 40% shorter than the interval suggested in the IEC standard. The DFT frequency grid step is $\Delta_f = 8$ Hz, while the finer frequency grid with an interpolation factor $P = 11$ is $\Delta'_f = 0.728$ Hz.

The test case adopted for this paper considers a waveform with eight components, namely four harmonics and four interharmonics. The latter are between 5% and 10% of the magnitude of the fundamental. The initial phase of each component is independently drawn from a random uniform distribution between 0 e 2π. In this controlled environment, the degree of sparsity is known in advance, namely $|S_h| = 16$, including image terms. In practice, with suitable information about the maximum harmonic order and the extent of interharmonic distortion, a reasonable guess can be arrived at.

As far as the algorithm is concerned, the results are independent of the nature, either current or voltage, of the analyzed waveform. Distortion levels considered in this example are more consistent with an experimental situation involving current waveforms, whereas smaller values would be involved in voltage harmonic and interharmonic analysis.

For this set of simulations, no additive broadband noise was included, as its effect is similar to what is already shown in Section III and further discussed in [21]. The analysis that follows is focused on the ability to detect and measure interharmonic components.

It should be noticed that harmonic magnitudes are larger than in the example of the previous section. Although possibly less realistic, this choice was made to stress-test support recovery performances for interharmonic components.

Table III refers to the case where all harmonic frequencies are located on the fine CS-DFT grid, thereby avoiding any interference with the much smaller interharmonic components. As the latter cannot instead be assumed to fall upon fine-grid points, the worst case has been considered, with frequencies falling exactly amidst two fine-grid points. Hence, the OMP support recovery step will point to approximate frequency locations for interharmonic components (within ± 0.364 Hz).

For the sake of simplicity, Table III does not report performance results for the harmonic components of the test waveform. Their positioning on the fine frequency grid ensures that they are exactly recovered, and therefore the same results presented in Table I apply to them. Furthermore, they do not interfere with the estimation of interharmonics.

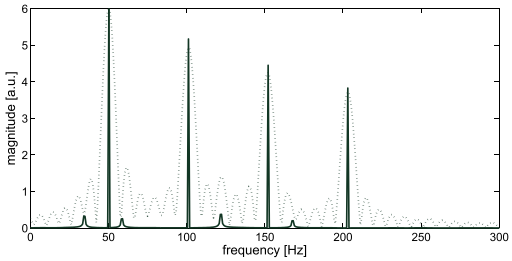

Fig. 2. CS-DFT analysis of a signal with harmonic and interharmonic contents. A zero-padded 256-point DFT (dotted) is plotted for comparison.

The algorithm correctly detects all interharmonic components achieving a satisfactory degree of accuracy, as shown by reported deviations from reference values in magnitude and phase. It should be remarked that scalloping loss effects with the CS-DFT algorithm are much smaller than in the standard DFT case. The resulting magnitude estimates are plotted in Fig. 2.

The quasi-coherent case can be analyzed by assuming 50 Hz as the fundamental frequency, which means a 0.5% deviation from the value given in Table III. As far as harmonic components are concerned, the results are similar to those already reported in Table II (actually slightly better, on account of the smaller off-grid offset) and will not be mentioned again.

For interharmonics, it should be reminded that the resolution required by the IEC standard is 5 Hz. It seems reasonable, therefore, to assume this as a minimum frequency separation, in particular, between an interharmonic and a neighboring harmonic component. In terms of the fine-grid step size given above, this distance is greater than $6 \cdot \Delta'_f$. In the very nearly coherent sampling conditions assumed for this test, the distance is large enough to ensure that interference caused by leakage from slightly off-grid harmonics is negligible. Therefore, the results given for interharmonics in Table III also apply in this case. In some instances, DFT record size N could be adjusted to help meet the large separation condition.

B. PMU—Phasor Measurement in Steady-State Conditions

With reference to PMUs, compliance trials for phasor measurements have been carried out reproducing all test conditions specified in IEEE Standard C37.118.1 [7]. The steady-state results are reported here, in terms of TVE, while the results for dynamic conditions are reported in the next section.

The total vector error (TVE) of a phasor measurement is defined as the relative difference between the phasor estimate and the theoretical phasor value of the signal being measured. Steady-state compliance requires that TVE should not exceed 1%. For the purposes of this paper, the only relevant difference between P-class and M-class devices concerns off-nominal frequency conditions, where a variability range of ± 2 Hz has to be allowed in the former case, while a range of ± 5 Hz is required for the M class.

TABLE IV
MAXIMUM AND RMS VALUES OF TVE FOR DIFFERENT SNR LEVELS

SNR	MAX	RMS
60 dB	2.7×10^{-4}	1.4×10^{-4}
50 dB	8×10^{-4}	4×10^{-4}
40 dB	3×10^{-3}	1×10^{-3}
30 dB	1×10^{-2}	5×10^{-3}
20 dB	3×10^{-2}	1×10^{-2}
10 dB	1.2×10^{-1}	6×10^{-2}

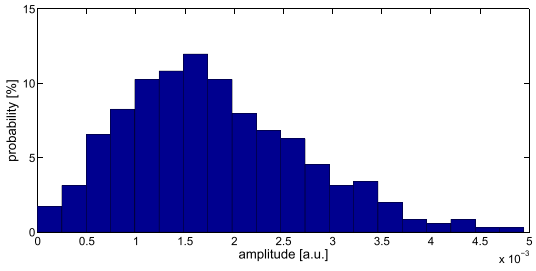

Fig. 3. Histogram of TVE for the case of Table IV and SNR = 30 dB.

The results discussed in this section refer to a data record size $N = 256$ samples. Sampling frequency is 5000 Hz, which corresponds to an observation interval of 51.2 ms. The DFT frequency grid step is $\Delta_f = 19.53$ Hz, while the finer frequency grid with an interpolation factor $P = 11$ is $\Delta'_f = 1.776$ Hz. It should be noted that phasor measurement refers to the fundamental frequency only, and therefore the OMP algorithm can be terminated after just one iteration. Referring to the first of the two stopping criteria mentioned in Section II, this means setting $t_{\mathrm{MAX}} = 1$.

As far as the effects of noise are concerned, support recovery is the critical part of the algorithm, as its task is to identify waveform components. Table IV reports the maximum and root-mean-square (RMS) values of TVE at different SNR levels. It is assumed that the fundamental frequency lies on the fine grid, so that only the effect of noise can be evidenced.

In the current OMP-based implementation, support detection becomes more difficult as the SNR drops below 20 dB [21]. This can be considered an acceptable performance limitation in power system measurement, with the possible exception of noise temporarily induced by transient phenomena, such as lightning strikes or the opening of circuit breakers. In a realistic phasor measurement context, SNR could be expected to remain around 40 dB or better.

TVE variability caused by the addition to waveform samples of white noise with 30 dB SNR is summarized in the histogram of Fig. 3. This shows an approximately Rayleigh distribution, in agreement with the fact that, as noted above, DFT coefficients are affected by complex Gaussian white noise.

Accuracy analysis follows straightforwardly by considering (11), where, since $t_{\mathrm{MAX}} = 1$, $\mathbf{D}_S$ is simply the vector $\mathbf{d}_{l_1}$ of the elements of $\mathbf{D}$ having the column index l_1 associated with the estimated fundamental frequency. Remembering (8), the estimate is

$$\hat{a}_{l_1} = \left(\mathbf{d}_{l_1}^H \mathbf{d}_{l_1}\right)^{-1} \mathbf{d}_{l_1}^H (\mathbf{s} + \mathbf{n}) \tag{12}$$

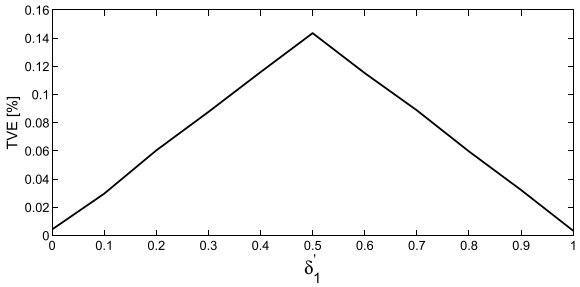

Fig. 4. Variation of maximum TVE, calculated for SNR = 40 dB, as a function of the normalized offset from the fine grid, δ'_1, of phasor frequency. The range of variation spans a full fine-grid step.

where the noise contribution from $\mathbf{n}$ has zero mean and variance $(\mathbf{d}_{l_1}^H \mathbf{d}_{l_1}) \cdot \sigma_n^2 / N = \sigma_n^2 / N$, the equality following from the fact that $\mathbf{d}_{l_1}^H \mathbf{d}_{l_1}$ is the equivalent noise bandwidth of the Dirichlet kernel, i.e., equal to one.

Assuming negligible interference from residual waveform components, in the neighborhood of l_1, the sum in (2) can be restricted to the fundamental, allowing to use for the DFT coefficients the simplified expression

$$S\left(\frac{k}{N}\right) = \frac{A_1}{2}\, e^{j\phi_1} D_N\left(\frac{k}{N} - \nu_1\right). \tag{13}$$

The deterministic part of (12) is then

$$\mathrm{E}[\hat{a}_{l_1}] = \frac{A_1}{2}\, e^{j\phi_1} \frac{\sum_{k=0}^{N-1} D_N^*\left(\frac{k}{N} - \frac{l_1}{N'}\right) D_N\left(\frac{k}{N} - \nu_1\right)}{\sum_{k=0}^{N-1} \left|D_N\left(\frac{k}{N} - \frac{l_1}{N'}\right)\right|^2} \tag{14}$$

where $D_N^*()$ is the complex conjugate of $D_N()$.

It follows from (14) that TVE depends on the value of δ'_1, which expresses the distance between ν_1 and l_1/NP as a fraction of the fine-grid step. The plot showing the maximum value of TVE versus δ'_1, for SNR = 40 dB, is shown in Fig. 4. It is clear that the possibility to better approximate frequency, because of the fine CS-DFT grid, allows to keep TVE comfortably below the 1% limit.

Tests were also carried out with regards to the effects of harmonic distortion and out-of-band interference. Since the proposed algorithm has very good frequency selectivity, these effects are easily bypassed. The resulting maximum TVE is below 0.03% for out-of-band interference and better than 0.015% for harmonic distortion.

V. PHASOR MEASUREMENT—DYNAMIC TEST CONDITIONS

Dynamic compliance requirements specified by IEEE Standard C37.118.1 include an extensive set of test conditions. In the following, unless otherwise specified, the same measurement configuration employed in Section IV is assumed. It should be remembered that, in this case, the reference phasor changes with time and, therefore, TVE will also be a time-varying quantity, whose value can be determined at reporting times t_r.

Assuming that the CS-DFT algorithm can process a continuous stream of samples in real time, so that no dead time occurs between consecutive records (this will depend on the

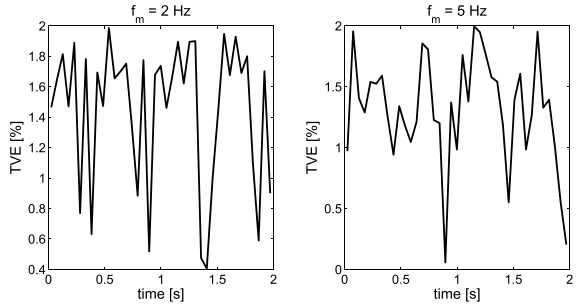

Fig. 5. TVE plots for dynamic compliance measurement bandwidth test.

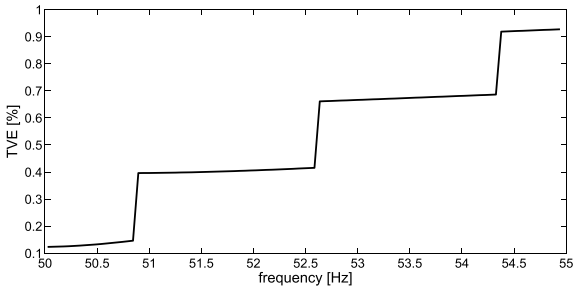

Fig. 6. Plot of TVE versus instantaneous frequency $f(t)$ for the frequency ramp test. Frequency range: 50–55 Hz.

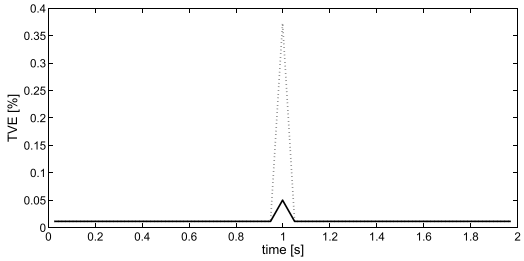

Fig. 7. TVE plots for magnitude (+10%) and phase ($+\pi/18$) step changes. Continuous line indicates magnitude step TVE, and dotted line indicates phase step TVE.

computing power actually available in the algorithm implementation), the maximum rate at which phasor measurements can be made available is $1/(NT_s)$. Since estimates obtained by a DFT algorithm are referenced to the center of the relevant sample record, the CS-DFT estimate at reporting time $t_r = r \cdot NT_s$ has to be compared with the reference phasor at time $(r - 1/2)\,NT_s$.

With these conventions, a number of TVE plots, referring to the different test conditions specified in the IEEE standard, have been determined to characterize the algorithm.

A. Amplitude and Phase Modulation

A test input with simultaneous amplitude and phase modulation is required to determine synchrophasor measurement bandwidth, according to [7]. For single-phase measurement, the test signal is defined by

$$s(t) = A[1 + k_x \cos(2\pi f_m t)] \times \cos[2\pi f_0 t + k_a \cos(2\pi f_m t - \pi)] \tag{15}$$

with $k_x = 0.1$ and $k_a = 0.1$ rad.

With the assumptions made above, the maximum reporting rate would be approximately 20 Hz. Modulation frequency f_m should be varied between 0.1 Hz and the maximum value of 2 Hz for P-class PMUs, while for M class devices, the maximum could be just one-fifth of the maximum reporting rate, i.e., 4 Hz. Nevertheless, simulation tests were still carried out up to 5 Hz and the results are reported for this higher frequency.

TVE requirements for measurement bandwidth are somewhat mitigated, an error not greater than 3% being allowed. Fig. 5 shows plots of TVE for two different values of modulation frequency, $f_m = 2$ and 5 Hz, calculated over a simulation time of 2 s. Although accuracy was found to progressively decrease as the rate of change of amplitude and phase gets higher, the algorithm complies with specifications for both M and P classes, with TVE never exceeding 2%.

B. Frequency Ramp

In the frequency ramp test, signal frequency is ramped either up or down while keeping amplitude constant. Starting from the nominal frequency f_0, the frequency range is either ± 2 or ± 5 Hz, respectively, for P- and M-class requirements. Instantaneous frequency is $f(t) = f_0 + R_f t$, with $R_f = 1$ Hz/s. The total frequency variation over an observation interval is $R_f \cdot NT_s$, which turns out to be rather limited, making this a quasi-stationary test input.

The TVE plot for an upramp from 50 to 55 Hz is shown in Fig. 6, similar results being obtained for the downward frequency ramp. Given the value of R_f, the simulation covers a time interval of 5 s, but it is more useful to indicate the corresponding instantaneous frequency on the abscyssa. It has to be remembered that signal frequency falls exactly on the fine grid whenever $f(t) = l \cdot \Delta'_f$, with $\Delta'_f = 1.776$ Hz.

It can be easily observed from Fig. 6 that TVE increases by steps whose corresponding width on the frequency abscyssa is exactly Δ'_f. By proper choice of the algorithm parameters, TVE in the neighborhood of the power-line frequency of interest can be kept below the required 1% limit.

C. Magnitude and Phase Step

In the step change test, the signal consists of a pure sinusoidal tone, whose magnitude or phase is given a step variation for which the standard specifies, respectively, a $\pm 10\%$ change or a ± 10 degrees ($\pi/18$ rad) phase shift. M and P classes require different response times, but are both required to keep TVE below 1%.

Fig. 7 shows that the algorithm complies with test requirements, remaining below the upper bound by almost an order of magnitude. The results refer to a $+10\%$ amplitude step and to a $+\pi/18$ phase step, plots for the corresponding negative steps being equal.

As can be expected with any DFT-based estimator, the effect of a step extends over twice the observation interval, i.e., slightly more than 100 ms in this instance. It is apparent

that a phase step has a much greater impact on TVE, yet this still remains well within specified bounds.

D. Experimental Validation

Analysis by numerical simulation usually allows thorough characterization of a measurement algorithm. Nevertheless, further validation by means of some test bench may still be desirable. The results are found to be extremely close to those presented above, confirming the correctness of the simulation setup employed in this paper.

Simpler tests, notably for step changes, were performed by generating voltage waveforms with an Agilent 6812B ac power source/power analyzer having an adjustable output voltage up to 300 V. Signals are acquired with a National Instruments NI-cDAQ 9188 unit equipped with a voltage module (National Instruments NI 9225, 24-bit resolution, ±300 Vrms, and sampling rate 50 kHz), and further processed by means of MATLAB code.

The measurement bandwidth test has been implemented by a low-voltage test bench, which allows full characterization of measurement algorithms while neglecting the impact on PMU performances of HV or MV voltage and/or current transducer accuracies. Required voltage waveforms are obtained by means of a set of three laboratory voltage generators controlled by a LabVIEW software application. A Hewlett–Packard 8904A signal generator provides the output waveform, and is connected to two Agilent 33220A waveform generators providing suitable modulation inputs. Samples are acquired through a National Instruments data acquisition module (NI USB-6211, 16-bit resolution, ±10 V, and sampling rate 250 kHz) and processed by means of MATLAB code, which yields TVE estimates at the desired reporting rate. Synchronization signals from the generators have also been recorded, for further processing and verification.

It should be noted that, in both systems, digitizer resolution is much higher than what was assumed in simulation analysis. Therefore, measurement variability can actually be lower than reported in the previous sections.

The results of the measurement bandwidth test are shown in Fig. 8. Each signal acquisition is 12-s long overall and consists of three portions. The first and last segment have a duration of 1 s and provide as a reference signal the unmodulated waveform in nominal conditions, i.e., a pure sinusoidal tone at 50 Hz with initial phase equal to zero. The middle portion, instead, contains the test specific perturbation for a length of 10 s. Modulation frequency f_m can range from 0.1 to 5 Hz, while modulation parameters are the same considered in the numerical experiment in Section V-A. The outcomes of simulation analysis are fully confirmed.

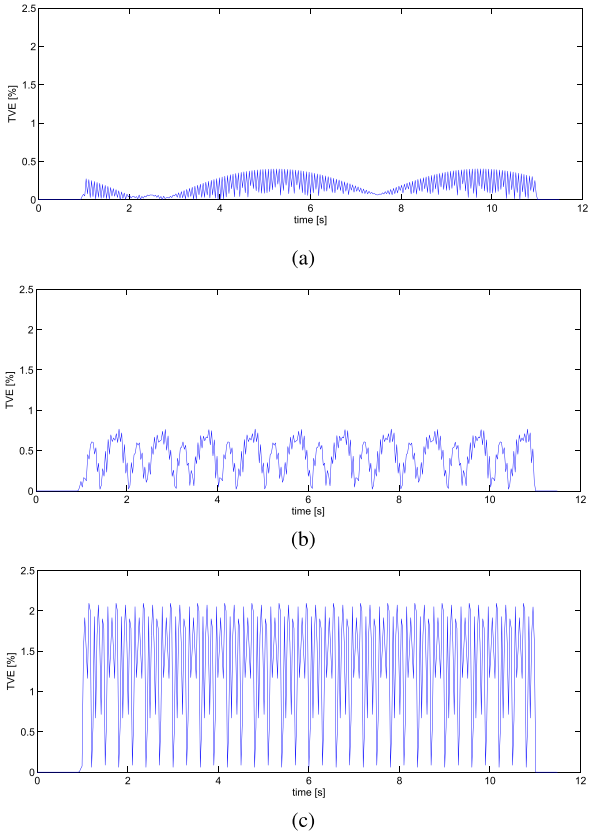

Fig. 8. TVE under combined amplitude and phase modulation at different modulation frequencies f_m. (a) $f_m = 0.1$ Hz. (b) $f_m = 1$ Hz. (c) $f_m = 5$ Hz.

VI. Conclusion

In the literature, DFT-based methods constitute a reference model for phasor measurement and power quality analysis. A thorough comparison is beyond the aim of this paper; however, it can be claimed that the combination of DFT and CS-based methods appears promising in achieving significant reductions of measurement time. Of course, computational complexity of the CS algorithm is higher than a simple DFT, but still within manageable limits for the processing capabilities of current equipment. In particular, computation of DFT coefficients by an FFT algorithm is a highly parallelizable task that can be implemented efficiently on a field-programmable gate array (FPGA) architecture. This allows to quickly process sample records, while possibly leaving to a main processor in the measuring equipment the CS algorithm. For phasor measurement, however, the single OMP iteration could as well find room within an FPGA.

Discussion of different measurements in this paper has shown that the CS-DFT algorithm is remarkably adaptable, allowing to easily trade speed for accuracy by simply changing the record length N. In PMU measurements, the moderate frequency separation requirement for a correct resolution of waveform components in any possible setting gives the possibility to keep the observation time well below two periods of the fundamental component. This in turn affects the choice of the number of samples in a record, N, for which the best solution should be a good compromise between peculiar application requirements and available computational power. The interpolation factor P can also be changed to some degree, adding a further possibility to optimize performance. By proper parameter settings, the algorithm could provide class M PMU accuracy at the faster reporting rate of class-P devices.

The main features of the proposed algorithm make it of interest for application in smart microgrid projects. Its basic

structure can be adapted to a range of PQA and PMU measurements by a comparatively simple set of management and control rules, while the underlying hardware may remain unchanged. This goes toward the aim of realizing low-cost high-performance measurement nodes in distribution-level smart microgrids, which are one of the targets of current research in the field.

From the viewpoint of complexity, the CS-DFT algorithm is more demanding than other DFT-based algorithms, but, for PMU measurement, it is arguably on a similar level as weighted least squares and dynamic Fourier-based algorithms, with the advantage that shorter observation intervals are allowed.

Short-time high-resolution waveform analysis is usually associated with parametric model-based methods, such as Pisarenko harmonic decomposition and its developments. As already noted, Prony's method, which has similar computational requirements to other model-based algorithms, has also been successfully applied to power system measurement [17]. While the CS-DFT algorithm is inferior in terms of accuracy, it may prove more adaptable for multifunction smart microgrid measurement.

Development of this paper will follow along two lines, pointing to the study of efficient and cost-effective implementations, as well as to better performing algorithms for support recovery and signal reconstruction. Capabilities of the approach at lower levels of voltage harmonic and interharmonic distortion need to be further investigated, in connection with phasor and waveform analysis. Further aspects requiring consideration are performances beyond the scenario outlined by the requirements of IEEE Std C37.118.1-2011, particularly in the more dynamic environment of distribution grids with distributed energy resources, for which the proposed CS-DFT algorithm should prove well suited.

REFERENCES

[1] C. Muscas, "Power quality monitoring in modern electric distribution systems," *IEEE Instrum. Meas. Mag.*, vol. 13, no. 5, pp. 19–27, Oct. 2010.

[2] G. D'Antona, C. Muscas, P. Pegoraro, and S. Sulis, "Harmonic source estimation in distribution systems," *IEEE Trans. Instrum. Meas.*, vol. 60, no. 10, pp. 3351–3359, Oct. 2011.

[3] D. Fabri, C. Martins, L. Silva, C. Duque, P. Ribeiro, and A. Cerqueira, "Time-varying harmonic analyzer prototype," in *Proc. 14th ICHQP*, Bergamo, Italy, Sep. 2010, pp. 1–7.

[4] T. Tarasiuk, "Comparative study of various methods of DFT calculation in the wake of IEC standard 61000-4-7," *IEEE Trans. Instrum. Meas.*, vol. 58, no. 10, pp. 3666–3677, Oct. 2009.

[5] A. G. Phadke, *Synchronized Phasor Measurements and Their Applications*. New York, NY, USA: Springer-Verlag, 2008, ch. 3.

[6] R. O. Burnett, M. M. Butts, and P. S. Sterlina, "Power system applications for phasor measurement units," *IEEE Comput. Appl. Power*, vol. 7, no. 1, pp. 8–13, Jan. 1994.

[7] *IEEE Standard for Synchrophasor Measurements for Power Systems*, IEEE Standard C37.118.1-2011, 2011.

[8] D. Belega, D. Dallet, and D. Petri, "Accuracy of sine wave frequency estimation by multipoint interpolated DFT approach," *IEEE Trans. Instrum. Meas.*, vol. 59, no. 11, pp. 2808–2815, Nov. 2010.

[9] M. Bertocco, C. Narduzzi, and F. Tramarin, "Characterization of microgrid smart metering: Phasor estimation under impaired conditions," in *Proc. IEEE I2MTC*, Minneapolis, MN, USA, May 2013, pp. 1170–1175.

[10] D. Macii, D. Petri, and A. Zorat, "Accuracy analysis and enhancement of DFT-based synchrophasor estimators in off-nominal conditions," *IEEE Trans. Instrum. Meas.*, vol. 61, no. 10, pp. 2653–2664, Oct. 2012.

[11] A. Testa *et al.*, "Interharmonics: Theory and modeling," *IEEE Trans. Power Del.*, vol. 22, no. 4, pp. 2335–2348, Oct. 2007.

[12] J. A. de la O Serna, "Dynamic phasor estimates for power system oscillations," *IEEE Trans. Instrum. Meas.*, vol. 56, no. 5, pp. 1648–1657, Oct. 2007.

[13] W. Premerlani, B. Kasztenny, and M. Adamiak, "Development and implementation of a synchrophasor estimator capable of measurements under dynamic conditions," *IEEE Trans. Power Del.*, vol. 23, no. 1, pp. 109–123, Jan. 2008.

[14] M. A. Platas-Garza and J. A. de la O Serna, "Dynamic harmonic analysis through Taylor–Fourier transform," *IEEE Trans. Instrum. Meas.*, vol. 60, no. 3, pp. 804–813, Mar. 2011.

[15] G. Barchi, D. Macii, and D. Petri, "Synchrophasor estimators accuracy: A comparative analysis," *IEEE Trans. Instrum. Meas.*, vol. 62, no. 5, pp. 963–973, May 2013.

[16] D. Belega and D. Petri, "Performance of synchrophasor measurements provided by the weighted least squares approach," in *Proc. IEEE I2MTC*, Minneapolis, MN, USA, May 2013, pp. 946–951.

[17] J. A. de la O Serna, "Synchrophasor estimation using Prony's method," *IEEE Trans. Instrum. Meas.*, vol. 62, no. 8, pp. 2119–2128, Aug. 2013.

[18] H. Farhangi, "The path of the smart grid," *IEEE Power Energy Mag.*, vol. 8, no. 1, pp. 18–28, Jan./Feb. 2010.

[19] N. Hatziargyriou, H. Asano, R. Iravani, and C. Marnay, "Microgrids," *IEEE Power Energy Mag.*, vol. 5, no. 4, pp. 78–94, Jul./Aug. 2007.

[20] M. Bertocco, G. Frigo, C. Narduzzi, and F. Tramarin, "Resolution enhancement in harmonic analysis by compressive sensing," in *Proc. IEEE Int. Workshop Appl. Meas. Power Syst. (AMPS)*, Aachen, Germany, Sep. 2013, pp. 40–45.

[21] M. Bertocco, G. Frigo, and C. Narduzzi, "On compressed sensing and super-resolution in DFT-based spectral analysis," in *Proc. 19th IMEKO TC-4 Symp. 17th IWADC Workshop Adv. Instrum. Sensors Interoperab.*, Barcelona, Spain, Jul. 2013.

[22] J. Schoukens and J. Renneboog, "Modeling the noise influence on the Fourier coefficients after a discrete Fourier transform," *IEEE Trans. Instrum. Meas.*, vol. IM-35, no. 3, pp. 278–286, Sep. 1986.

[23] Y. C. Pati, R. Rezaiifar, and P. S. Krishnaprasad, "Orthogonal matching pursuit: Recursive function approximation with applications to wavelet decomposition," in *Proc. 27th Annu. Asilomar Conf. Signals, Syst. Comput.*, vol. 1. Pacific Grove, CA, USA, Nov. 1993, pp. 40–44.

[24] J. A. Tropp and A. C. Gilbert, "Signal recovery from random measurements via orthogonal matching pursuit," *IEEE Trans. Inf. Theory*, vol. 53, no. 12, pp. 4655–4666, Dec. 2007.

Matteo Bertocco (M'87) received the Laurea and Ph.D. degrees in electronics engineering from the University of Padova, Padova, Italy, in 1991.

He has been a Researcher with the Department of Electronics and Informatics, University of Padova, since 1994, and became an Associate Professor of Electronic Instrumentation and Measurement in 1998 and a Full Professor in 2002. He is the Director of the Ph.D. School in Information Engineering. He has authored over 130 technical papers published in international journals and conference proceedings. His current research interests include wireless sensor networks, automated instrumentation, and electromagnetic compatibility.

Dr. Bertocco has been a Research Associate Member of the Institute of Electronics, Computer and Telecommunication Engineering, National Research Council, Rome, Italy, since 2011.

Guglielmo Frigo received the master's degree in biomedical engineering, from the University of Padova, Padova, Italy. He is currently pursuing the Ph.D. degree with the Department of Information Engineering, University of Padova, Padova, Italy.

He joined the Electronic Measurement Research Group in 2011. His current research interests include compressive sensing, superresolution, and phasor measurements on power systems for smart microgrid applications.

Claudio Narduzzi (S'79–M'83) was born in Venice, Italy, in 1958. He received the Laurea (*cum laude*) degree in electronics engineering from the University of Padova, Padova, Italy, in 1982.

He is a Full Professor of Instrumentation and Measurement with the School of Engineering, University of Padova, where he was the Director of Taught Programs in Electronics Engineering from 2008 to 2012. He has been involved in several instrumentation-related topics in the areas of electronics and telecommunications, including spectral analysis, inverse filtering, circuit testing, quantization, and analog-to-digital conversion. He has authored over 150 scientific papers and textbooks for academic courses. His current research interests include networked measuring systems, and digital signal processing applications in measurement, instrumentation, and test system characterization.

Federico Tramarin (S'07–M'12) received the master's degree in electronic engineering and the Ph.D. degree in information engineering from the University of Padova, Padova, ltaly, in 2008 and 2012, respectively.

In 2012 he worked as a Post-Doctoral Researcher with the Electronic Measurement research group. at the same University. He is currently a Post-Doctoral Research Assistant with the National Research Council - Institute of Electronics, Computer and Telecommunication Engineering, Padova, Italy.

His current research interests include distributed measurement systems, wireless sensor networks, and performance measurements on real-time (wired/wireless) networks.